nature communications

Article

https://doi.org/10.1038/s41467-026-72811-z

Fermi-surface diagnosis for topological superconductivity with *s*-wave-like pairing symmetries

Received: 24 August 2025

Accepted: 24 April 2026

Published online: 25 May 2026

Check for updates

Zhongyi Zhang [1], Ken Shiozaki[2], Chen Fang [3,4] & Seishiro Ono [5,6] ✉

Theoretical prediction of topological superconductivity is key to their discovery. Recently, it is proven that in 199 out of 230 space groups, topological superconductivity coexists with an *s*-wave-like pairing symmetry, raising the hope of finding more candidates for this exotic phase. However, a comprehensive and efficient method for diagnosing topological superconductivity in realistic materials remains elusive. Here, we derive Fermi-surface formulas for gapped and gapless topological phases of time-reversal symmetric superconductors with *s*-wave-like pairing symmetries in all layer and space groups, applicable to thin-film and bulk materials. Our diagnosis uses only the sign of the pairing and the Fermi velocity at several Fermi points, and yields complete (partial) diagnosis for gapped and gapless superconducting phases in 159 (71) space groups. This provides a fundamental basis for the first-principles prediction of new topological superconductors.

Over the past decades, the discovery of materials exhibiting bulk topological superconductivity has been one of the central issues in condensed matter physics[1–5]. Thanks to intensive studies in recent years, it has been shown that a wide variety of topological superconducting phases exist[6–25]. Unconventional superconductors, such as *p*- and *d*-wave superconductors, serve as important platforms for realizing topological superconductivity[26–41]. However, such non-*s*-wave superconductors are rare in nature. As a consequence, we have not yet verified the existence of intrinsic topological superconductivity in real materials.

Recently, a class of time-reversal symmetric spinful superconductors has been extensively studied[42–56]. In these superconductors, the Cooper pairs are invariant under all spatial symmetry operations for a given space group. We refer to a time-reversal symmetric spinful superconductor with this property as "superconductor with *s*-wave-like pairing symmetry" (more precise definition is provided below). Notably, most ever-discovered superconductors fall into this class. It is natural to ask how many topological phases exist in this class. In fact, this question is answered by classification of gapped topological superconducting phases in all space groups. It turns out that topological superconductivity is compatible with *s*-wave-like pairing symmetries in 199 out of the 230 space groups[45]. Importantly, all nontrivial gapped phases in this class exhibit topologically protected gapless states on boundaries. More recently, ref. 46 has found topological invariants defined for Bogoliubov-de Gennes (BdG) Hamiltonians, which can characterize gapped and gapless superconductors in this class. Despite these advances, it remains challenging to compute topological invariants for realistic materials following these definitions, as full BdG Hamiltonians are often unavailable for realistic superconductors.

The theories of symmetry indicators and topological quantum chemistry have been introduced to efficiently detect nontrivial topology in insulators and semimetals[57–62]. Moreover, symmetry-indicator theory has been generalized to superconductors[63–66], enabling the diagnosis of topology in realistic superconductors using only irreducible representations of normal-state wave functions and pairing

[1]Department of Physics, Hong Kong University of Science and Technology, Clear Water Bay, Hong Kong, China. [2]Center for Gravitational Physics and Quantum Information, Yukawa Institute for Theoretical Physics, Kyoto University, Kyoto, Japan. [3]Beijing National Laboratory for Condensed Matter Physics, and Institute of Physics, Chinese Academy of Sciences, Beijing, China. [4]Kavli Institute for Theoretical Sciences, Chinese Academy of Sciences, Beijing, China. [5]RIKEN Center for Interdisciplinary Theoretical and Mathematical Sciences (iTHEMS), RIKEN, Wako, Japan. [6]Institute for Solid State Physics, University of Tokyo, Kashiwa, Japan. ✉e-mail: s-ono@g.ecc.u-tokyo.ac.jp

symmetries under certain assumptions[67]. However, this approach fails for s-wave-like pairings: all topologically nontrivial phases with s-wave-like pairing symmetries cannot be detected by existing symmetry indicators [see Supplementary Note 2A for more details]. Thus, an efficient diagnostic framework for the topology with s-wave-like pairing symmetries remains elusive.

In this work, we present Fermi-surface formulas of topological invariants in all layer and space groups, applicable to both thin-film and bulk materials. Importantly, all our formulas require only signs of the Fermi velocities and intraband pairings on line segments connecting two high-symmetry points—no information about the entire Fermi surfaces is needed (see Fig. 1 for an illustration). In addition to the efficiency, our formulas can detect a wide range of nontrivial topological phases—including both gapped and gapless—with s-wave-like pairing symmetries. Our formulas provide a complete efficient diagnosis of gapped and stable gapless phases in 159 space groups and partial coverage in the remaining 71 space groups.

Results

Fermi surface formulas

In this work, we focus on s-wave-like pairing symmetries, formally defined by the symmetry properties of the order parameter $\Delta_{\mathbf{k}}$. Let $U_{\mathbf{k}}(g)$ be a representation of a space group symmetry g. We say that the pairing symmetry is s-wave-like if $U_{\mathbf{k}}(g)\Delta_{\mathbf{k}}U^{\top}_{-\mathbf{k}}(g)=\Delta_{g\mathbf{k}}$ for all symmetries in a given space group. It should be noted that the s-wave-like pairing symmetry does not necessarily mean that the system is a conventional s-wave superconductor. For example, consider a single orbital superconducting order $\Delta_{\mathbf{k}}=(\mathbf{d}(\mathbf{k})\cdot\boldsymbol{\sigma})i\sigma_y$ under the mirror symmetry $\mathcal{M}_z$ along the z-axis, where $\mathbf{d}(\mathbf{k})=(0,\mathrm{i}\sin k_x,0)$ and $\sigma_{i=0,x,y,z}$ are Pauli matrices in spin space. While this is p-wave like, the pairing symmetry is s-wave like, as one can see $\mathrm{i}\sigma_z\Delta_{\mathbf{k}}(\mathrm{i}\sigma_z)^{\top}=\Delta_{\mathcal{M}_z\mathbf{k}}$. Another representative example is $s_{\pm}$-wave pairing.

Topological invariants are often defined on subregions in momentum space. For convenience, we decompose the Brillouin zone into points, line segments, and polygons in a symmetric manner[68,69]. See Fig. 2(b) for an illustration of the decomposition. We assign an orientation to each component. For example, line segment a in Fig. 2(b) is oriented from Γ to X. In this work, we consider topological invariants defined on the line segments.

Before presenting our main results on the Fermi surfaces of the topological invariants, we introduce our basic assumptions on target systems. We always assume that superconductors are in the weak coupling regime. More precisely, we assume that the target superconducting system can be continuously deformed into a superconductor that possesses the following properties:

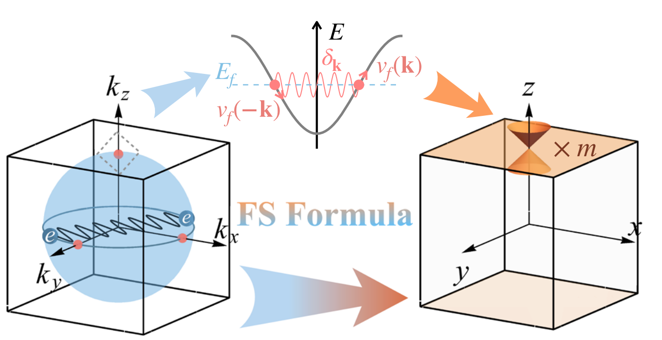

Fig. 1 | Illustration of our Fermi-surface formulas. On the left-hand side, the red dots represent intersections of the Fermi surface with certain line segments in the Brillouin zone. All we need for the formulas are the signs of Fermi velocities, v_f and intraband pairings, $\delta_{\mathbf{k}}$ at the intersections. Our formulas enable us to compute topological invariants only from the information at the intersections. Nonzero values of the invariants indicate the existence of some gapless states on boundaries, as illustrated by the example on the right-side[21,86].

(i) intraband pairings dominate, i.e., all interband pairings are negligible;
(ii) the superconducting gap is negligible except on Fermi surfaces.

In addition, we further assume that the following conditions are satisfied:

(iii) all Fermi surfaces are minimally degenerate as allowed by symmetries;
(iv) normal state energies at high-symmetry points are not at the Fermi level;
(v) there is no superconducting node on all line segments, including their endpoints.

The assumptions (iii) and (iv) usually hold for realistic systems. The assumption (v) must be satisfied to define topological invariants on line segments.

Under these five assumptions, intraband pairing potentials and Fermi velocities can determine the values of topological invariants defined on the line segments. To define intraband pairing potentials and Fermi velocities, we consider the m-th Fermi point at $\mathbf{k}_m$ and momenta $\mathbf{k}$ in its neighborhood. Let $\Phi^{\alpha}_{\mathbf{k},m}$ be a matrix whose columns are eigenvectors of the normal conducting Hamiltonian $h_{\mathbf{k}}$ with the energy $\varepsilon^{\alpha}_{\mathbf{k},m}$, where α is a label of an irreducible representation (irrep) $u^{\alpha}_{\mathbf{k}}(g)$. In other words, $\Phi^{\alpha}_{\mathbf{k},m}$ satisfies the relations $h_{\mathbf{k}}\Phi^{\alpha}_{\mathbf{k},m}=\varepsilon^{\alpha}_{\mathbf{k},m}\Phi^{\alpha}_{\mathbf{k},m}$ and $U_{\mathbf{k}}(g)\Phi^{\alpha}_{\mathbf{k},m}=\Phi^{\alpha}_{\mathbf{k},m}u^{\alpha}_{\mathbf{k}}(g)$. Then, the intraband pairing potential is defined by a projected superconducting order

$$\tilde{\Delta}^{\alpha}_{\mathbf{k},m}:=[\Phi^{\alpha}_{\mathbf{k},m}]^{\dagger}\Delta_{\mathbf{k}}[U(\mathcal{T})]^{*}\Phi^{\alpha}_{\mathbf{k},m}. \tag{1}$$

Here, $U(\mathcal{T})$ is a unitary representation of time-reversal symmetry (TRS) satisfying $U(\mathcal{T})[U(\mathcal{T})]^{*}=-\mathbb{1}$, where $\mathbb{1}$ is the identity matrix. The above intraband pairing satisfies the relations

$$[\tilde{\Delta}^{\alpha}_{\mathbf{k},m}]^{\dagger}=\tilde{\Delta}^{\alpha}_{\mathbf{k},m};\ \ u^{\alpha}_{\mathbf{k}}(g)\tilde{\Delta}^{\alpha}_{\mathbf{k},m}[u^{\alpha}_{\mathbf{k}}(g)]^{\dagger}=\tilde{\Delta}^{\alpha}_{\mathbf{k},m}. \tag{2}$$

Since $u^{\alpha}_{\mathbf{k}}(g)$ is irreducible, the intraband pairing is proportional to the identity matrix. In particular, when we consider the Fermi point $\mathbf{k}_m$ on the line segment l, we represent $\tilde{\Delta}^{\alpha}_{\mathbf{k}_m,m}$ by

$$\tilde{\Delta}^{\alpha}_{\mathbf{k}_m,m}=\delta^{(l,\alpha)}_{m}\mathbb{1}\ \ (\delta^{(l,\alpha)}_{m}\in\mathbb{R}), \tag{3}$$

where $\delta^{(l,\alpha)}_{m}$ represents the intraband pairing potential at the m-th Fermi point with irrep α on line segment l.

The Fermi velocity is defined by the directional derivative of the energy. Suppose that we consider a line segment l connecting from $\mathbf{k}_{\mathrm{A}}$ to $\mathbf{k}_{\mathrm{B}}$, and that the m-th Fermi point at $\mathbf{k}_m$ lies on this line segment. The Fermi velocity of the energy $\varepsilon^{\alpha}_{\mathbf{k},m}$ is given by

$$v^{(l,\alpha)}_{m}:=\nabla_{\mathbf{k}}\varepsilon^{\alpha}_{\mathbf{k},m}|_{\mathbf{k}=\mathbf{k}_m}\cdot\hat{\mathbf{e}}_l, \tag{4}$$

where $\hat{\mathbf{e}}_l=(\mathbf{k}_{\mathrm{B}}-\mathbf{k}_{\mathrm{A}})/\parallel\mathbf{k}_{\mathrm{B}}-\mathbf{k}_{\mathrm{A}}\parallel$.

Based on these two quantities, we define a set of integer-valued quantities $\{\mathcal{N}_{(l,\alpha)}\}_{l,\alpha}$ for a given system:

$$\mathcal{N}_{(l,\alpha)}:=\sum_{m=1}^{n_{(l,\alpha)}}\mathrm{sgn}(v^{(l,\alpha)}_{m})\frac{1-\mathrm{sgn}\,(\delta^{(l,\alpha)}_{m})}{2}\in\mathbb{Z}, \tag{5}$$

where $n_{(l,\alpha)}$ is the number of minimally degenerate Fermi points with irrep α on line segment l. In fact, this integer-valued quantity encodes the topological nature of superconducting phases under the above assumptions.

Now, we are ready to provide concrete forms of Fermi-surface formulas of topological invariants. For each space group, there exist three types of topological invariants: (i) $\mathbb{Z}$-valued invariants

 https://doi.org/10.1038/s41467-026-72811-z

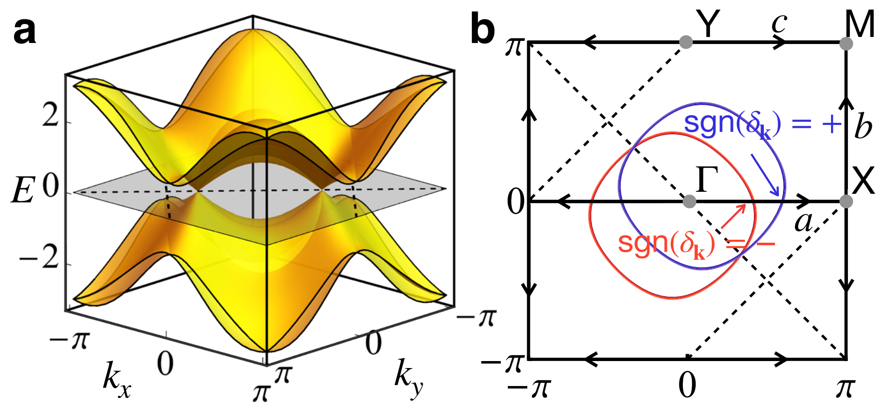

Fig. 2 | Illustration of the model (10) and (11). **a** shows the energy dispersion of the BdG Hamiltonian (11). **b** shows decomposition of the Brillouin zone, Fermi surfaces (colored solid lines), and the pairing nodes (dashed lines). The solid black lines and arrows denote the line segments specified by the gray endpoints and their orientations. The red and blue colors in the figure indicate Fermi surfaces with mirror eigenvalues + i and − i, respectively. The intersections of the Fermi surface and the pairing nodes correspond to the gapless points in (**a**). The parameters are set to be $\{t, \lambda, \mu, \Delta\} = \{-1, 0.3, -1, 0.3\}$.

$\{\mathcal{W}_i^{\text{gapless}}\}_{i=1}^{N_{\text{gapless}}}$ to detect gapless points in two-dimensional subregions surrounded by line segments; (ii) $\mathbb{Z}$-valued invariants $\{\mathcal{W}_i^{\text{gapped}}\}_{i=1}^{N_{\text{gapped}}}$ to capture gapped topological phases; (iii) $\mathbb{Z}_\lambda$-valued invariants $\{\mathcal{X}_i\}_{i=1}^{M}$ to identify gapped topological phases. It should be emphasized that both the number of defined topological invariants (N_{gapless}, N_{gapped}, M), and topological invariants themselves depend on a given space group. Notably, gapped topological phases detected by $\{\mathcal{W}_i^{\text{gapped}}\}_{i=1}^{N_{\text{gapped}}}$ and $\{\mathcal{X}_i\}_{i=1}^{M}$ must have protected gapless surface states. Furthermore, $\{\mathcal{W}_i^{\text{gapless}}\}_{i=1}^{N_{\text{gapless}}}$ can detect all stable gapless phases in all space groups with *s*-wave-like pairing symmetries (See Supplementary Note 2 for more details).

Our Fermi-surface formulas of these invariants are given by

$$\begin{aligned}\mathcal{W}_i^{\text{gapless}} &= \sum_{l,\alpha} w_{i,(l,\alpha)}^{\text{gapless}} \mathcal{N}_{(l,\alpha)} \\ &= \sum_{l,\alpha} w_{i,(l,\alpha)}^{\text{gapless}} \sum_{m=1}^{n_{(l,\alpha)}} \text{sgn}(v_m^{(l,\alpha)}) \frac{1-\text{sgn}\,(\delta_m^{(l,\alpha)})}{2},\end{aligned} \tag{6}$$

$$\begin{aligned}\mathcal{W}_i^{\text{gapped}} &= \sum_{l,\alpha} w_{i,(l,\alpha)}^{\text{gapped}} \mathcal{N}_{(l,\alpha)} \\ &= \sum_{l,\alpha} w_{i,(l,\alpha)}^{\text{gapped}} \sum_{m=1}^{n_{(l,\alpha)}} \text{sgn}(v_m^{(l,\alpha)}) \frac{1-\text{sgn}\,(\delta_m^{(l,\alpha)})}{2},\end{aligned} \tag{7}$$

$$\begin{aligned}\mathcal{X}_i &= \sum_{l,\alpha} x_{i,(l,\alpha)} \mathcal{N}_{(l,\alpha)} \bmod \lambda \\ &= \sum_{l,\alpha} x_{i,(l,\alpha)} \sum_{m=1}^{n_{(l,\alpha)}} \text{sgn}(v_m^{(l,\alpha)}) \frac{1-\text{sgn}\,(\delta_m^{(l,\alpha)})}{2} \bmod \lambda,\end{aligned} \tag{8}$$

where $w_{i,(l,\alpha)}^{\text{gapless}}, w_{i,(l,\alpha)}^{\text{gapped}}, x_{i,(l,\alpha)} \in \mathbb{Z}$ represent contribution weights of irrep α on line segment l for topological invariants. In other words, these integer-valued quantities tell us about two important things: which line segments and irreps are relevant for topological invariants, and how we should combine Fermi-point data $\{\mathcal{N}_{(l,\alpha)}\}_{l,\alpha}$ to detect the topological nature of superconducting phases. For a given space group, we can systematically determine these contribution weights by Atiyah-Hirzebruch spectral sequence. See ref. 46 for more details. For $\mathbb{Z}_2$-valued invariants, we can drop $\text{sgn}\,(v_m^{(l,\alpha)})$ since $n = -n \bmod 2$ for an integer n. As a result, the formulas can be further simplified to

$$\mathcal{X}_i = \sum_{l,\alpha} x_{i,(l,\alpha)} \sum_{m=1}^{n_{(l,\alpha)}} \frac{1-\text{sgn}\,(\delta_m^{(l,\alpha)})}{2} \bmod 2. \tag{9}$$

These formulas immediately give us the following insight. The quantities (6)–(9) are always trivial for superconductors whose intraband pairings have the same sign everywhere. This means that superconductors in the BCS limit, which can be connected to the vacuum without closing gap, cannot have nontrivial values of Eqs. (6)–(9).

We make three remarks on our formulas. First, our Fermi-surface formulas are well-defined for a given decomposition, including the orientations of line segments, of the Brillouin zone in a space group. In Supplementary Information, we provide our formulas together with all line segments we used for all layer groups and space groups. If we adopt a different decomposition, we may have physically equivalent but different forms of the formulas. This is because changing the decomposition can change the contribution weights in general. Next, topological invariants for gapped phases, $\{\mathcal{W}_i^{\text{gapped}}\}_{i=1}^{N_{\text{gapped}}}$ and $\{\mathcal{X}_i\}_{i=1}^{M}$, are meaningful only when invariants for gapless points, $\{\mathcal{W}_i^{\text{gapless}}\}_{i=1}^{N_{\text{gapless}}}$, are all trivial. Lastly, topological invariants defined on higher-dimensional subspaces would be required for gapped topological phases that cannot be detected by our formulas. For example, detecting the nonzero three-dimensional winding number $w_{3\text{D}} \in \mathbb{Z}$ requires information on the entire three-dimensional Brillouin zone[70]. Nonetheless, our Fermi surface formula can still detect $w_{3\text{D}} \bmod n$ (where n depends on the space group), as seen below. This is similar to the situation for symmetry indicators[57,58,71].

Examples

Here, we demonstrate how it works through three theoretical models constructed by the real-space construction method and one realistic model from real material.

First, we consider a quasi-two-dimensional gapless superconductor in the layer group $p11m$. This layer group is generated by the mirror symmetry $\mathcal{M}_z = \{M_z|(000)\}$ and translation symmetries along x- and y-direction. The decomposition of the Brillouin zone is shown in Fig. 2(b). The normal state Hamiltonian for the superconductor is

$$h_{\mathbf{k}} = t(\cos k_x + \cos k_y)s_0 + \lambda(\sin k_x + \sin k_y)s_3, \tag{10}$$

and the corresponding BdG Hamiltonian takes the form

$$H_{\mathbf{k}}^{\mathrm{BdG}} = [h_{\mathbf{k}} - \mu]\kappa_3 + \Delta_{\mathrm{sc}}(\sin k_x + \sin k_y)s_1\kappa_1, \tag{11}$$

where the Pauli matrices s_j and κ_j ($j = 0, 1, 2, 3$) stand for spins and the Nambu spinor. In addition to TRS and mirror symmetry $\mathcal{M}_z$, the BdG Hamiltonian inherently possesses particle-hole symmetry $\mathcal{C}$. For the above BdG Hamiltonian, their representations are given by

$$U^{\mathrm{BdG}}(\mathcal{T}) = \mathrm{i}s_2,\ U^{\mathrm{BdG}}(\mathcal{C}) = \kappa_1,\ U^{\mathrm{BdG}}(\mathcal{M}_z) = \mathrm{i}\kappa_3 s_3. \tag{12}$$

The pairing term $\Delta_{\mathbf{k}} = \Delta_{\mathrm{sc}}(\sin k_x + \sin k_y)s_1$ remains invariant under mirror symmetry $\mathcal{M}_z$: $U_{\mathbf{k}}(\mathcal{M}_z)\Delta_{\mathbf{k}}U_{\mathbf{k}}^{\top} = \Delta_{\mathcal{M}_z\mathbf{k}}$, where $U_{\mathbf{k}}(M_z)$ is the representation of the mirror symmetry in the normal phase. Therefore, the pairing exhibits the s-wave-like pairing symmetry. As shown in Fig. 2(a), the energy spectrum of $H_{\mathbf{k}}^{\mathrm{BdG}}$(11) has two superconducting gapless points.

Our formula for $\mathbb{Z}$-valued invariants can detect these gapless points. Using Eq. (6), we find the formula

$$\begin{aligned}\mathcal{W}_1^{\mathrm{gapless}} = \sum_{\alpha=\pm}\alpha\Bigg[&\sum_{m=1}^{n_{(c,\alpha)}}\mathrm{sgn}(v_m^{(c,\alpha)})\frac{1-\mathrm{sgn}\,(\delta_m^{(c,\alpha)})}{2}\\ &-\sum_{m=1}^{n_{(a,\alpha)}}\mathrm{sgn}(v_m^{(a,\alpha)})\frac{1-\mathrm{sgn}\,(\delta_m^{(a,\alpha)})}{2}\Bigg],\end{aligned} \tag{13}$$

where $\alpha = \pm$ means the mirror eigenvalue $\pm\,\mathrm{i}$ for eigenstates of the normal state Hamiltonian (10). The signs of Fermi velocities $v^{(a,\pm)}$ on the line segment a are positive. According to the sign of $\delta_{\mathbf{k}}$ shown in Fig. 2(b), we have $\mathcal{W}^{\mathrm{gapless}} = -1$. In fact, the invariant is equivalent to the mirror winding number defined on a loop $(-\pi, 0) \to (\pi, 0) \to (\pi, \pi) \to (-\pi, \pi) \to (-\pi, 0)$. The nontrivial mirror winding number indicates the existence of gapless points inside the loop[72].

Next, we consider a gapped topological superconductor (TSC) in layer group $p2_1/b11$ to show that our formulas can be used even when the formula in ref. 70 cannot. Generators of this layer group are glide symmetry $\mathcal{G}_x = \{M_x|(\frac{1}{2}\frac{1}{2}0)\}$, inversion symmetry $\mathcal{I} = \{I|(000)\}$, and translation symmetry along x-direction. In the presence of inversion symmetry and TRS, Fermi surfaces in spinful electronic systems must be at least twofold degenerate. Furthermore, topological invariants for class DIII in the tenfold classification[73–75] are also trivial for even-parity pairings. Therefore, this symmetry setting is out of the scope of ref. 70.

Here, we describe our model in which there are four sublattice degrees of freedom labeled by $(\tau_z, \sigma_z) = (\pm 1, \pm 1)$. Their coordinates in a unit cell are specified by $(x, y) = \frac{1}{4}[(2-\tau_z)(1,0) + (1-\sigma_z)(0,1)]$ [see Fig. 3(a)]. According to ref. 45, the classification of gapped topological phases is $\mathbb{Z}_2$, whose generator is constructed by placing one-dimensional TSCs along $x = 1/4$ and $x = 3/4$ in each unit cell. To realize this, we consider a model whose normal state Hamiltonian is given by

$$h_{\mathbf{k}} = t(\Gamma_{010} + \cos k_y\Gamma_{010} + \sin k_y\Gamma_{020}), \tag{14}$$

and the BdG Hamiltonian is

$$H_{\mathbf{k}}^{\mathrm{BdG}} = [h_{\mathbf{k}} - \mu]\kappa_3 + 2\Delta_{\mathrm{sc}}\sin k_y\Gamma_{301}\kappa_1, \tag{15}$$

where $\Gamma_{ijk} := \tau_i \otimes \sigma_j \otimes s_k (i, j, k = 0, 1, 2, 3)$. As mentioned above, the minimal degeneracy of states is twofold at each momentum. However, the Fermi surfaces of $h_{\mathbf{k}}$ in Eq. (14) are fourfold degenerate, which violates assumption (iii), as indicated by the gray dashed lines in Fig. 3(b). This violation can be easily resolved by introducing symmetry-allowed perturbations that are small enough not to change any topology, as shown by the solid gray lines in Fig. 3(b).

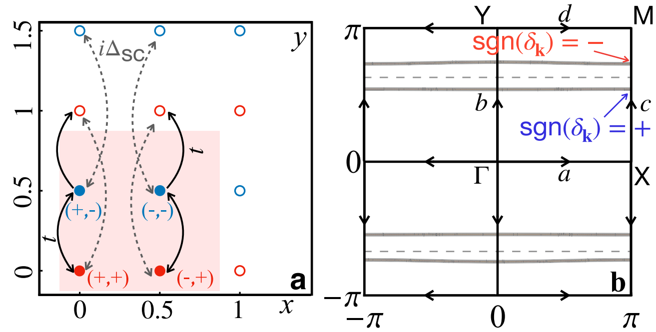

Fig. 3 | Illustration of the model in layer group $p2_1/b11$. a Real-space description of the model. The red shaded region indicates the unit cell. The red and blue solid circles denote the four sublattices labeled by $(\tau_z, \sigma_z) = (\pm 1, \pm 1)$ in the unit cell. The solid (dashed) arrows represent the hopping between the sublattice degrees in the normal (pairing) part of the BdG Hamiltonian (15). **b** Fermi surfaces for the Hamiltonian (14). The gray solid (dashed) lines show the normal-state Fermi surfaces with (without) symmetry-allowed perturbations. The red and blue colors mean states with glide eigenvalue $+ie^{-ik_y/2}$ and $-ie^{-ik_y/2}$, respectively. The parameters are set to be $\{t, \mu\} = \{-1, 1\}$.

The $\mathbb{Z}_2$ topology can be diagnosed by our formula for $\mathbb{Z}_2$-valued invariant in Eq. (9). The decomposition of the Brillouin zone is shown in Fig. 3(b). Then, the formula is given by

$$\mathcal{X}_1 = \sum_{\alpha=\pm}\sum_{m=1}^{n_{(c,\alpha)}}\frac{1-\mathrm{sgn}(\delta_m^{(c,\alpha)})}{2} + \sum_{\beta=\pm}\sum_{m=1}^{n_{(d,\beta)}}\frac{1-\mathrm{sgn}\,(\delta_m^{(d,\beta)})}{2}, \tag{16}$$

where $\alpha = \pm$ represents the glide eigenvalue $\pm\mathrm{i}e^{-ik_y/2}$ on the line segment c, and $\beta = \pm$ denotes the screw symmetry $\mathcal{S}_x = \mathcal{G}_x\mathcal{I}$ eigenvalue $\pm\mathrm{i}e^{-ik_x/2}$ on the line segment d. According to the sign of $\delta_{\mathbf{k}}$ shown in Fig. 3(b), we have $\mathcal{X} = 1 \bmod 2$.

Last, we discuss a strong TSC in space group $P4_1$ to show that our formula can inform the three-dimensional winding number $w_{3\mathrm{D}}$ modulo four. This space group is generated by fourfold screw symmetry $\mathcal{S}_{4z} = \{C_{4z}|(00\frac{1}{4})\}$ and translation symmetries along x- and y-directions.

Our model is described as follows. There are four sublattice degrees of freedom in a unit cell, whose coordinates in a unit cell are $(x, y, z) = (0, 0, 0)$, $(0, 0, 1/4)$, $(0, 0, 1/2)$, and $(0, 0, 3/4)$, labeled as 1, 2, 3, and 4, respectively. The normal state Hamiltonian is constructed as

$$\begin{aligned}\hat{\mathcal{H}}_0 = &\sum_{s,\mathbf{R}}\sum_{i=1}^{4} -\frac{t}{2}(\hat{c}^{\dagger}_{si\mathbf{R}+\mathbf{a}}\hat{c}_{si\mathbf{R}} + \hat{c}^{\dagger}_{si\mathbf{R}+\mathbf{b}}\hat{c}_{si\mathbf{R}}) + h.c.\\ &+\sum_{s,\mathbf{R}} -\frac{t}{2}(\hat{c}^{\dagger}_{s1\mathbf{R}}\hat{c}_{s2\mathbf{R}} + \hat{c}^{\dagger}_{s2\mathbf{R}}\hat{c}_{s3\mathbf{R}} + \hat{c}^{\dagger}_{s4\mathbf{R}}\hat{c}_{s3\mathbf{R}}) + h.c.\\ &+\sum_{s,\mathbf{R}} -\frac{t}{2}\hat{c}^{\dagger}_{s4\mathbf{R}+\mathbf{c}}\hat{c}_{s1\mathbf{R}} + h.c.,\ \sum_{s,\mathbf{R},i}\hat{c}^{\dagger}_{si\mathbf{R}+\mathbf{c}}\hat{c}_{si\mathbf{R}},\end{aligned} \tag{17}$$

where the $\hat{c}_{si\mathbf{R}}$ ($\hat{c}^{\dagger}_{si\mathbf{R}}$) is the annihilation (creation) operator of an electron at the i-th sublattice with spin s in the unit cell at $\mathbf{R}$. Also, $\mathbf{a}$, $\mathbf{b}$, and $\mathbf{c}$ are the primitive lattice vectors along x-, y-, and z-direction, respectively. The pairing term is given by

$$\begin{aligned}\hat{\Delta} = &\sum_{s,\mathbf{R}} -\frac{i}{2}\Delta_{\mathrm{sc}}(\hat{c}^{\dagger}_{s1\mathbf{R}}\hat{c}^{\dagger}_{\bar{s}2\mathbf{R}} + \hat{c}^{\dagger}_{s4\mathbf{R}}\hat{c}^{\dagger}_{\bar{s}3\mathbf{R}} + \hat{c}^{\dagger}_{s2\mathbf{R}}\hat{c}^{\dagger}_{\bar{s}3\mathbf{R}}) + h.c.\\ &+\sum_{s,\mathbf{R}}\frac{i}{2}\Delta_{\mathrm{sc}}(\hat{c}^{\dagger}_{s1\mathbf{R}}\hat{c}^{\dagger}_{\bar{s}4\mathbf{R}+\mathbf{c}} - \sum_{i=1}^{4}s\hat{c}^{\dagger}_{si\mathbf{R}}\hat{c}^{\dagger}_{\bar{s}i\mathbf{R}+\mathbf{a}}) + h.c.\\ &+\sum_{s,\mathbf{R}}\sum_{i=1}^{4}\frac{1}{2}\Delta_{\mathrm{sc}}\hat{c}^{\dagger}_{si\mathbf{R}}\hat{c}^{\dagger}_{\bar{s}i\mathbf{R}+\mathbf{b}} - h.c.\end{aligned} \tag{18}$$

https://doi.org/10.1038/s41467-026-72811-z

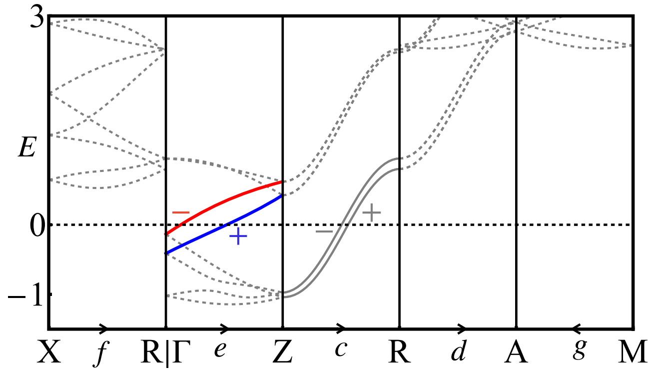

Fig. 4 | The band structure of the model (17) with symmetry-allowed perturbations in space group $P4_1$. Solid lines (dashed lines) represent bands crossing (not crossing) the Fermi level. The arrows represent the positive direction of the line segments c, d, e, f, and g. The red and blue colors mean states with screw eigenvalue $e^{-i(3\pi+k_z)/4}$ and $e^{-i(\pi+k_z)/4}$, respectively. The $+$ and $-$ represent the sign of $\delta_{\mathbf{k}}$ at the corresponding Fermi point. The parameters are set to be $\{t, \mu\} = \{1, 1.8\}$.

with s and $\bar{s}$ being the opposite spin. It is easy to check the system described by $\hat{\mathcal{H}}_{\mathrm{BdG}} = \hat{\mathcal{H}}_0 + \hat{\Delta}$ has the nonzero three-dimensional winding number $w_{3\mathrm{D}} = 1$.

Here, we compute the $\mathbb{Z}_8$-valued invariant by our formula (8):

$$\begin{aligned}\mathcal{X}_3 = &\sum_{l=e,g}\sum_{\alpha=1,3,5,7}(4-\alpha)\sum_{m=1}^{n_{(l,\alpha)}}\mathrm{sgn}(v_m^{(l,\alpha)})\frac{1-\mathrm{sgn}\,(\delta_m^{(l,\alpha)})}{2}\\ &+\sum_{l=c,d}\sum_{m=1}^{n_l}\mathrm{sgn}\,(v_m^l)(1-\mathrm{sgn}\,(\delta_m^l))\\ &+\sum_{\beta=\pm}\beta\sum_{m=1}^{n_{(f,\beta)}}\mathrm{sgn}\,(v_m^{(f,\beta)})(1-\mathrm{sgn}\,(\delta_m^{(f,\beta)})),\end{aligned} \tag{19}$$

where for line segment l = e and g, $v_m^{(l,\alpha)}$ and $\delta_m^{(l,\alpha)}$ $(\alpha = 1,3,5,7)$ are defined for screw eigenvalue $e^{-i(\alpha\pi+k_z)/4}$; for line segment f, $v_m^{(f,\beta)}$ and $\delta_m^{(f,\beta)}$ $(\beta = \pm)$ are defined for twofold rotation eigenvalues βi. After adding symmetry allowed perturbations to lift the accidental degeneracy in $\hat{\mathcal{H}}_0$, the energy spectrum is as shown in Fig. 4. According to the sign of $\delta_{\mathbf{k}}$ shown in Fig. 4, we find $\mathcal{X}_3 = 3$. In Methods, we show that $\mathcal{X}_3$ mod 4 serves as a $\mathbb{Z}_4$-valued indicator of $w_{3\mathrm{D}}$.

Application to realistic materials

We discuss $CaFeAs_2$, whose space group is $P2_1$, to demonstrate how to apply our formula to realistic materials based on first-principles calculations.

In Fig. 5, we show the band structure and Fermi surfaces obtained by DFT calculations. From the raw data of Fig. 5(a), we notice that there are eight Fermi surfaces around the Γ point and four Fermi surfaces around the M point. This implies that although the Fermi surfaces in Fig. 5(b) and (c) seem to be degenerate, there is no Fermi surface degeneracy. This is consistent with the symmetry analysis.

One can see that the k_z-dependence of Fermi surfaces is sufficiently weak, and topological properties inherit the quasi-two-dimensional nature of its electronic structure. Therefore, we focus on k_z = 0 plane with the exchange of k_x- and k_y-axes to illustrate the workflow of our diagnostic scheme, which results in Layer group $p2_111$ (No. 9).

According to our Fermi surface formula, there exist a $\mathbb{Z}$-valued invariant for gapless points, a $\mathbb{Z}_2$-valued invariant, and a $\mathbb{Z}_4$-valued invariant, whose expressions are given by

$$\begin{aligned}\mathcal{W}_1^{\mathrm{gapless}} = &\sum_{m=1}^{n_{a_1}}\mathrm{sgn}(v_m^{a_1})\frac{1-\mathrm{sgn}(\delta_m^{a_1})}{2}+\sum_{m=1}^{n_{a_2}}\mathrm{sgn}(v_m^{a_2})\frac{1-\mathrm{sgn}(\delta_m^{a_2})}{2}\\ &-\sum_{m=1}^{n_{b_1}}\mathrm{sgn}(v_m^{b_1})\frac{1-\mathrm{sgn}\,(\delta_m^{b_1})}{2}+2\sum_{m=1}^{n_{c_1}}\mathrm{sgn}(v_m^{c_1})\frac{1-\mathrm{sgn}\,(\delta_m^{c_1})}{2}\\ &-\sum_{m=1}^{n_{d_1}}\mathrm{sgn}(v_m^{d_1})\frac{1-\mathrm{sgn}(\delta_m^{d_1})}{2}-\sum_{m=1}^{n_{d_2}}\mathrm{sgn}(v_m^{d_2})\frac{1-\mathrm{sgn}\,(\delta_m^{d_2})}{2};\end{aligned} \tag{20}$$

$$\mathcal{X}_1 = \sum_{m=1}^{n_{b_1}}\frac{1-\mathrm{sgn}(\delta_m^{b_1})}{2}+\sum_{m=1}^{n_{d_1}}\frac{1-\mathrm{sgn}(\delta_m^{d_1})}{2}+\sum_{m=1}^{n_{d_2}}\frac{1-\mathrm{sgn}\,(\delta_m^{d_2})}{2}\ \mathrm{mod}\ 2; \tag{21}$$

$$\begin{aligned}\mathcal{X}_2 = &\,2\sum_{m=1}^{n_{a_2}}\mathrm{sgn}(v_m^{a_2})\frac{1-\mathrm{sgn}(\delta_m^{a_2})}{2}-\sum_{m=1}^{n_{b_1}}\mathrm{sgn}(v_m^{b_1})\frac{1-\mathrm{sgn}(\delta_m^{b_1})}{2}\\ &-2\sum_{m=1}^{n_{d_1}}\mathrm{sgn}(v_m^{d_1})\frac{1-\mathrm{sgn}\,(\delta_m^{d_1})}{2}\ \mathrm{mod}\ 4.\end{aligned} \tag{22}$$

Here, a_1 and d_1 (a_2 and d_2) are symbols of the irreducible representations whose character of screw symmetry along x-axis is $-\mathrm{i}e^{-\mathrm{i}k_x/2}$ ($+\mathrm{i}e^{-\mathrm{i}k_x/2}$) (see Section L9 in Supplementary Information for more detailed information).

As a demonstration, here we discuss some scenarios out of all possibilities, in which sign changes happen between the Fermi surfaces near the M point while fixing the pairing signs of the Fermi surfaces near the Γ point to be positive. Although a global gauge transformation can give rise to the global minus sign of the superconducting order parameter, this does not affect the topology. As a result, there are six inequivalent pairing sign choices for possible fully gapped superconducting states (whose $\mathcal{W}_1^{\mathrm{gapless}}$ must be trivial), as shown in Fig. 6(b–g). According to the formulas of the invariants, we find that four of these configurations correspond to topologically nontrivial states, $(\mathcal{W}_1^{\mathrm{gapless}}, \mathcal{X}_1, \mathcal{X}_2) = (0, 0, 2)$. This phase is equivalent to x-direction stacking copies of one-dimensional class DIII topological superconductors along the y-direction, as shown in Fig. 6(h) (see Supplementary Note 3A for more details). The model in Fig. 6(h) with a small perturbation is a second-order topological superconductor with Majorana corner modes, as shown in Fig. 6(i).

Finally, let us return to the discussion of the three-dimensional nature. Due to its quasi-two-dimensional electronic nature, three-dimensional topological properties can be understood by stacking the aforementioned two-dimensional topological states along the z-direction. As a result, we conclude that this three-dimensional topological phase exhibits hinge modes along the z-direction.

Discussion

We introduce Fermi-surface formulas of topological invariants for time-reversal symmetric superconductors with s-wave-like pairing symmetries in all layer and space groups. Most of the superconductors ever discovered belong to this class, and within it, many potential candidates for topological superconductors remain to be verified, such as iron-based superconductors[76], nickelate-based superconductors[77,78], highly overdoped CuO_2 monolayer[79] and heavy fermion superconductors[80]. This new method requires minimal information on the material, namely the sign of pairing and Fermi velocity at several Fermi points, and yet provides complete topological properties for 159 space groups. While our diagnosis for gapped phases remains partial for 71 space groups, a large part of the nontrivial phases can still be detected.

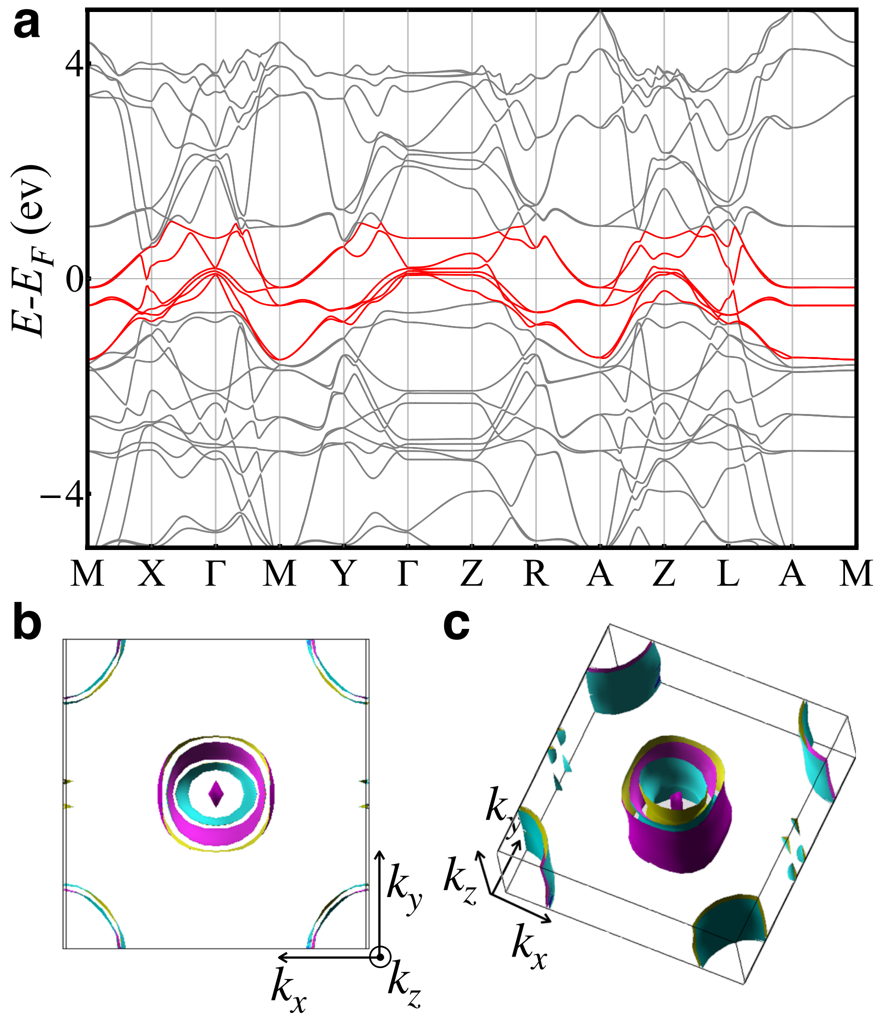

Fig. 5 | First-principle calculation results for $CaFeAs_2$. a The band structure of $CaFeAs_2$. The bands near the Fermi energy E_F are marked in red. M, X, Γ, Y, Z, R, A, L represent $(\pi/2, \pi/2, 0)$, $(\pi/2, 0, 0)$, $(0, 0, 0)$, $(0, \pi/2, 0)$, $(0, 0, \pi/2)$, $(0, \pi/2, \pi/2)$, $(\pi/2, \pi/2, \pi/2)$, $(\pi/2, 0, \pi/2)$ in the Brillouin zone, respectively. **b**, **c** The Fermi surface of $CaFeAs_2$ with different viewpoints. The Fermi surfaces are visualized by XCrySDen[87].

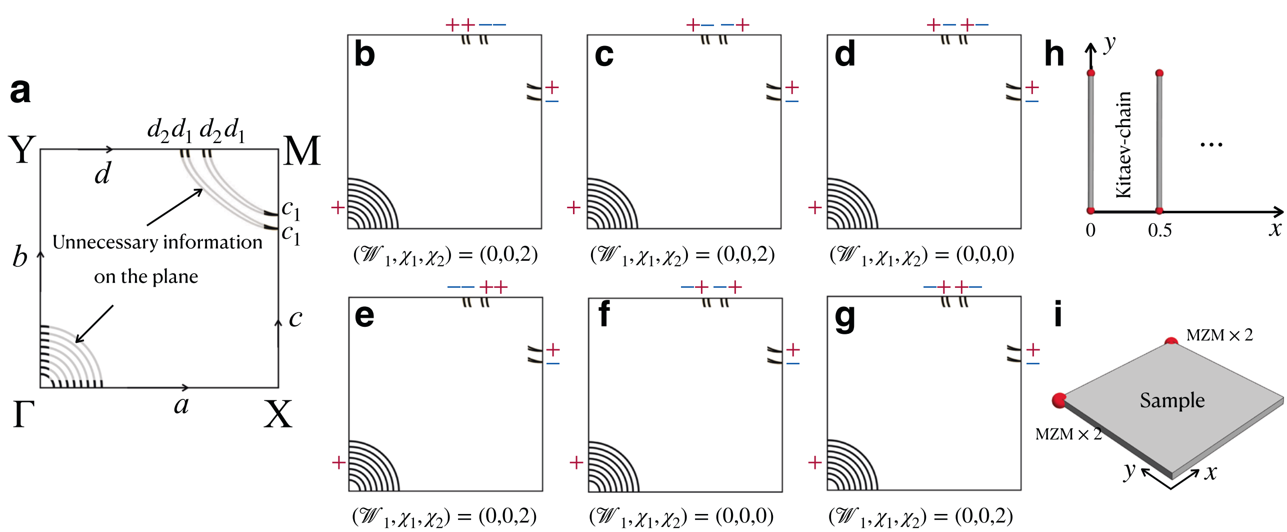

Fig. 6 | Demonstration of our diagnosis of topological phases based on first-principles calculation results. a Fermi surface of quasi-2D $CaFeAs_2$ based on the DFT-calculated data. a, b, c, d are the one-cell, whose directions are labeled by arrows. c_i and d_i represent the irreducible representations on the one-cell c and d. Γ, X, Y, M represent $(0, 0)$, $(\pi, 0)$, $(0, \pi)$ and (π, π). **b**–**g** The six inequivalent pairing sign configurations satisfying $\mathcal{W}_1^{\text{gapless}} = 0$. + and − represent the pairing sign δ_i^l of i-th Fermi points on the line segment l. $\mathcal{W}$, $\mathcal{X}_1$ and $\mathcal{X}_2$ represent the value of the topological invariants defined in Eqs. (20), (21) and (22). **h** The real-space construction of the topological nontrivial state with $(\mathcal{W}, \mathcal{X}_1, \mathcal{X}_2) = (0, 0, 2)$. **i** The corner modes of the topological nontrivial state with $(\mathcal{W}, \mathcal{X}_1, \mathcal{X}_2) = (0, 0, 2)$.

 https://doi.org/10.1038/s41467-026-72811-z

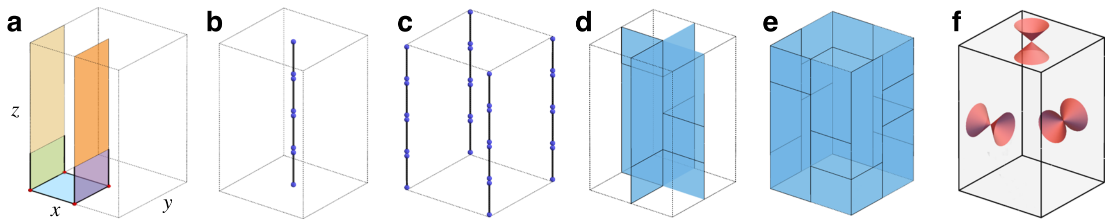

Fig. 7 | Illustration of real-space constructions of representative topological superconducting phases in $P4_1$. a Unit cell and its cell complex for space group $P4_1$ (No. 76). The dashed lines denote the unit cell. The symmetry-inequivalent 2-cells, 1-cells and 0-cells are represented as colored faces, bold line segments, and red dots, respectively. The other cells can be obtained from them by acting with symmetry operations in SG $P4_1$. **b**, **c** Two generators of $\mathbb{Z}_2^2$-topological phases constructed from 1D TSCs. The black bold lines represent the nontrivial 1D TSCs in DIII class, and the blue dots represent the corresponding Majorana zero modes at the endpoints of 1D TSCs. **d**, **e** Two generators of $\mathbb{Z}_2^2$ constructed from 2D TSCs. The blue faces represent the nontrivial 2D TSCs in DIII class. The regions enclosed by solid lines represent the decorations on the symmetry-inequivalent 2-cells. **f** The illustration for the strong TSC in DIII class.

Table 1 | The quantitative mappings between all representative models and the topological invariants ($\mathcal{W}_1^{\text{gapless}}, \mathcal{W}_2^{\text{gapless}}, \mathcal{X}_1, \mathcal{X}_2, \mathcal{X}_3$) computed by our Fermi surface formula

Classification of ref. 45	w_{3D}	$(\mathcal{W}_1^{\text{gapless}}, \mathcal{W}_2^{\text{gapless}})$	$(\mathcal{X}_1, \mathcal{X}_2, \mathcal{X}_3)$
1D TSCs: $(1, 0) \in \mathbb{Z}_2 \times \mathbb{Z}_2$	0	(0, 0)	(1, 2, 4)
1D TSCs: $(0, 1) \in \mathbb{Z}_2 \times \mathbb{Z}_2$	0	(0, 0)	(1, 0, 4)
2D TSCs: $(1, 0) \in \mathbb{Z}_2 \times \mathbb{Z}_2$	0	(0, 0)	(0, 3, 4)
2D TSCs: $(0, 1) \in \mathbb{Z}_2 \times \mathbb{Z}_2$	0	(0, 0)	(0, 1, 0)
Strong TSC: $1 \in \mathbb{Z}$	1	(0, 0)	(1, 1, 3)

Here, $\mathcal{W}_1^{\text{gapless}}$ and $\mathcal{W}_2^{\text{gapless}}$ are $\mathbb{Z}$-valued invariants; $\mathcal{X}_1$, $\mathcal{X}_2$, and $\mathcal{X}_3$ are $\mathbb{Z}_2$-, $\mathbb{Z}_4$- and $\mathbb{Z}_8$-valued ones. The formulas are listed in Supplementary Information.

We emphasize the distinction between our formulas and the existing formulas introduced in refs. 70,81. They introduce formulas for class DIII without any spatial symmetries and for the one-dimensional winding number, respectively. In their derivation, they assume that there is no Fermi surface degeneracy. However, this assumption is often invalid in the presence of space group symmetries, where such Fermi surface degeneracy occurs. In addition, space group symmetries often prevent certain topological invariants from being nontrivial. For example, topological invariants in the scope of ref. 70 are always trivial for even-parity pairings with inversion symmetry. On the other hand, our formulas can detect nontrivial topology even in such cases, as shown in Sec. " Examples." Thus, our formulas have broader applicability than refs. 70,81.

Furthermore, the diagnostic scheme proposed in this work identifies a broader range of topological phases based on much less information on the superconductor than all previous works. In Sec. "Application to realistic materials," we actually demonstrate the effectiveness of our formulas by applying them to a density functional theory (DFT) calculation for a realistic material. Given the success of large-scale investigations of topological insulators using symmetry indicators and topological quantum chemistry[60–62], we anticipate that our formulas will play a crucial role in the discovery of realistic topological superconductors.

Methods

Relation between $\mathcal{X}_3$ and w_{3D}

Here, we argue that an odd value of $\mathcal{X}_3$ indicates oddness of w_{3D}. To show this, we compute $\mathcal{X}_3$ for all representatives of topological phases. In addition to the strong TSC, we have $(\mathbb{Z}_2)^2$ phases constructed from one-dimensional TSCs and $(\mathbb{Z}_2)^2$ phases constructed from two-dimensional TSCs[45], whose illustrations are shown in Fig. 7. In the Supplementary Note 3, we calculate all the gapless and gapped topological invariants for all representative models for these phases, which are summarized in Table 1. We find that all models with $w_{3D} = 0$ have $\mathcal{X}_3 = 0 \mod 4$. Also, we find $\mathcal{X}_3 = -w_{3D} \mod 4$ for the generator of strong TSCs. Therefore, we conclude that $\mathcal{X}_3 \mod 4$ faithfully reflects $w_{3D} \mod 4$. This argument can be generalized to $Pn_1 (n = 2, 3, 4, 6)$. In Supplementary Note 4, we show that our invariants provide a $\mathbb{Z}_2$-valued indicator of w_{3D} in $P2_1$ and a $\mathbb{Z}_6$-valued indicator for $P3_1$ and $P6_1$.

Detailed information on DFT calculations

In our DFT calculations, we employ QUANTUM ESPRESSO[82,83] and `qeirreps`[84] to obtain irreducible representations defined on line segments. The k-mesh is chosen as 24 × 24 × 24 in our self-consistent field calculations. The lattice structure is obtained from Cambridge Crystallographic Data Center (CCDC 961741)[85] for $La_xCa_{1-x}FeAs_2$[76] by taking $x = 0$.

Data availability

All data needed to evaluate the conclusions in the study are present in the paper and/or the Supplementary Information.

Code availability

The computer code used for numerical calculation and theoretical analysis is not publicly available because of the high cost of preparation and maintenance. It is available upon request from the corresponding authors.

References

1. Kitaev, A. Y. Unpaired Majorana fermions in quantum wires. *Phys. Uspekhi* **44**, 131 (2001).
2. Nayak, C. et al. Non-Abelian anyons and topological quantum computation. *Rev. Mod. Phys.* **80**, 1083 (2008).
3. Qi, X.-L. & Zhang, S.-C. Topological insulators and superconductors. *Rev. Mod. Phys.* **83**, 1057 (2011).
4. Alicea, J. New directions in the pursuit of Majorana fermions in solid state systems. *Rep. Prog. Phys.* **75**, 076501 (2012).
5. Sato, M. & Ando, Y. Topological superconductors: a review. *Rep. Prog. Phys.* **80**, 076501 (2017).

6. Das, A. et al. Zero-bias peaks and splitting in an Al–InAs nanowire topological superconductor as a signature of Majorana fermions. *Nat. Phys.* **8**, 887 (2012).
7. Machida, T. et al. Zero-energy vortex bound state in the superconducting topological surface state of Fe (Se, Te). *Nat. Mater.* **18**, 811 (2019).
8. Nadj-Perge, S. et al. Observation of Majorana fermions in ferromagnetic atomic chains on a superconductor. *Science* **346**, 602 (2014).
9. Zhang, P. et al. Observation of topological superconductivity on the surface of an iron-based superconductor. *Science* **360**, 182 (2018).
10. Morimoto, T. & Furusaki, A. Topological classification with additional symmetries from Clifford algebras. *Phys. Rev. B* **88**, 125129 (2013).
11. Wu, X. et al. Boundary-obstructed topological high-T_c superconductivity in iron pnictides. *Phys. Rev. X* **10**, 041014 (2020).
12. Yang, G., Stano, P., Klinovaja, J. & Loss, D. Majorana bound states in magnetic skyrmions. *Phys. Rev. B* **93**, 224505 (2016).
13. Shiozaki, K. & Sato, M. Topology of crystalline insulators and superconductors. *Phys. Rev. B* **90**, 165114 (2014).
14. Shiozaki, K., Sato, M. & Gomi, K. Topology of nonsymmorphic crystalline insulators and superconductors. *Phys. Rev. B* **93**, 195413 (2016).
15. Cornfeld, E. & Chapman, A. Classification of crystalline topological insulators and superconductors with point group symmetries. *Phys. Rev. B* **99**, 075105 (2019).
16. Geier, M., Trifunovic, L., Hoskam, M. & Brouwer, P. W. Second-order topological insulators and superconductors with an order-two crystalline symmetry. *Phys. Rev. B* **97**, 205135 (2018).
17. Wu, X., Qin, S., Liang, Y., Fan, H. & Hu, J. Topological characters in $Fe(Te_{1-x}Se_x)$ thin films. *Phys. Rev. B* **93**, 115129 (2016).
18. Trifunovic, L. & Brouwer, P. W. Higher-order bulk-boundary correspondence for topological crystalline phases. *Phys. Rev. X* **9**, 011012 (2019).
19. Cornfeld, E. & Carmeli, S. Tenfold topology of crystals: Unified classification of crystalline topological insulators and superconductors. *Phys. Rev. Res.* **3**, 013052 (2021).
20. Shiozaki, K. The classification of surface states of topological insulators and superconductors with magnetic point group symmetry. *Prog. Theor. Exp. Phys.* **2022**, 04A104 (2022).
21. Zhang, Z., Ren, J., Qi, Y. & Fang, C. Topological classification of intrinsic three-dimensional superconductors using anomalous surface construction. *Phys. Rev. B* **106**, L121108 (2022).
22. Simon, S., Geier, M. & Brouwer, P. W. Higher-order topological semimetals and nodal superconductors with an order-two crystalline symmetry. *Phys. Rev. B* **106**, 035105 (2022).
23. Zhang, Z. et al. Topological superconductivity from unconventional band degeneracy with conventional pairing. *Nat. Commun.* **15**, 7971 (2024).
24. Ono, S. & Shiozaki, K. Symmetry-based approach to superconducting nodes: unification of compatibility conditions and gapless point classifications. *Phys. Rev. X* **12**, 011021 (2022).
25. Zhang, Z. et al. Double Majorana vortex flat bands in the topological Dirac superconductor. *Commun. Phys.* **9**, 11 (2026).
26. Sato, M. Topological properties of spin-triplet superconductors and Fermi surface topology in the normal state. *Phys. Rev. B* **79**, 214526 (2009).
27. Sato, M. Topological odd-parity superconductors. *Phys. Rev. B* **81**, 220504(R) (2010).
28. Fu, L. & Berg, E. Odd-parity topological superconductors: theory and application to $Cu_xBi_2Se_3$. *Phys. Rev. Lett.* **105**, 097001 (2010).
29. Fischer, M. H. et al. Chiral *d*-wave superconductivity in SrPtAs. *Phys. Rev. B* **89**, 020509 (2014).
30. Matano, K. et al. Spin-singlet superconductivity with a full gap in locally noncentrosymmetric SrPtAs. *Phys. Rev. B* **89**, 140504(R) (2014).
31. Fu, L. Odd-parity topological superconductor with nematic order: application to $Cu_xBi_2Se_3$. *Phys. Rev. B* **90**, 100509(R) (2014).
32. Yanase, Y. Nonsymmorphic Weyl superconductivity in UPt_3 based on E_{2u} representation. *Phys. Rev. B* **94**, 174502 (2016).
33. Kawakami, T., Okamura, T., Kobayashi, S. & Sato, M. Topological crystalline materials of $J = 3/2$ electrons: antiperovskites, dirac points, and high winding topological superconductivity. *Phys. Rev. X* **8**, 041026 (2018).
34. Ishizuka, J. & Yanase, Y. Periodic Anderson model for magnetism and superconductivity in UTe_2. *Phys. Rev. B* **103**, 094504 (2021).
35. Jiao, L. et al. Chiral superconductivity in heavy-fermion metal UTe_2. *Nature* **579**, 523 (2020).
36. Venderbos, J. W. F., Savary, L., Ruhman, J., Lee, P. A. & Fu, L. Pairing states of spin-$\frac{3}{2}$ fermions: symmetry-enforced topological gap functions. *Phys. Rev. X* **8**, 011029 (2018).
37. Ahn, J. & Yang, B.-J. Higher-order topological superconductivity of spin-polarized fermions. *Phys. Rev. Res.* **2**, 012060 (2020).
38. Wu, X., Yang, F., Le, C., Fan, H. & Hu, J. Triplet p_z-wave pairing in quasi-one-dimensional $A_2Cr_3As_3$ superconductors (A = K, Rb, Cs). *Phys. Rev. B* **92**, 104511 (2015).
39. Khim, S. et al. Field-induced transition within the superconducting state of $CeRh_2As_2$. *Science* **373**, 1012 (2021).
40. Landaeta, J. F. et al. Field-angle dependence reveals odd-parity superconductivity in $CeRh_2As_2$. *Phys. Rev. X* **12**, 031001 (2022).
41. Yu, J., Chen, Y.-A. & Das Sarma, S. Euler-obstructed Cooper pairing: nodal superconductivity and hinge Majorana zero modes. *Phys. Rev. B* **105**, 104515 (2022).
42. Qi, X.-L., Hughes, T. L., Raghu, S. & Zhang, S.-C. Time-reversal-invariant topological superconductors and superfluids in two and three dimensions. *Phys. Rev. Lett.* **102**, 187001 (2009).
43. Zhang, F., Kane, C. L. & Mele, E. J. Time-reversal-invariant topological superconductivity and Majorana Kramers pairs. *Phys. Rev. Lett.* **111**, 056402 (2013).
44. Qin, S., Fang, C., Zhang, F.-C. & Hu, J. Topological superconductivity in an extended s-wave superconductor and its implication to iron-based superconductors. *Phys. Rev. X* **12**, 011030 (2022).
45. Ono, S., Shiozaki, K. & Watanabe, H. Classification of time-reversal symmetric topological superconducting phases for conventional pairing symmetries. *Phys. Rev. B* **109**, 214502 (2024).
46. Ono, S. & Shiozaki, K. Towards complete characterization of topological insulators and superconductors: A systematic construction of topological invariants based on Atiyah-Hirzebruch spectral sequence. https://arxiv.org/abs/2311.15814 (2024).
47. Béri, B. Topologically stable gapless phases of time-reversal-invariant superconductors. *Phys. Rev. B* **81**, 134515 (2010).
48. Haim, A., Keselman, A., Berg, E. & Oreg, Y. Time-reversal-invariant topological superconductivity induced by repulsive interactions in quantum wires. *Phys. Rev. B* **89**, 220504 (2014).
49. Deng, S., Viola, L. & Ortiz, G. Majorana modes in time-reversal invariant *s*-wave topological superconductors. *Phys. Rev. Lett.* **108**, 036803 (2012).
50. Scheurer, M. S. Mechanism, time-reversal symmetry, and topology of superconductivity in noncentrosymmetric systems. *Phys. Rev. B* **93**, 174509 (2016).
51. Haim, A. & Oreg, Y. Time-reversal-invariant topological superconductivity in one and two dimensions. *Phys. Rep.* **825**, 1 (2019).
52. Hosur, P., Dai, X., Fang, Z. & Qi, X.-L. Time-reversal-invariant topological superconductivity in doped Weyl semimetals. *Phys. Rev. B* **90**, 045130 (2014).

53. Wang, J., Xu, Y. & Zhang, S.-C. Two-dimensional time-reversal-invariant topological superconductivity in a doped quantum spin-Hall insulator. *Phys. Rev. B* **90**, 054503 (2014).
54. Zhang, R.-X. & Das Sarma, S. Intrinsic time-reversal-invariant topological superconductivity in thin films of iron-based superconductors. *Phys. Rev. Lett.* **126**, 137001 (2021).
55. Mellars, E. & Béri, B. Signatures of time-reversal-invariant topological superconductivity in the Josephson effect. *Phys. Rev. B* **94**, 174508 (2016).
56. Keselman, A., Fu, L., Stern, A. & Berg, E. Inducing time-reversal-invariant topological superconductivity and fermion parity pumping in quantum wires. *Phys. Rev. Lett.* **111**, 116402 (2013).
57. Po, H. C., Vishwanath, A. & Watanabe, H. Symmetry-based indicators of band topology in the 230 space groups. *Nat. Commun.* **8**, 50 (2017).
58. Bradlyn, B. et al. Topological quantum chemistry. *Nature* **547**, 298 (2017).
59. Kruthoff, J., de Boer, J., van Wezel, J., Kane, C. L. & Slager, R.-J. Topological classification of crystalline insulators through band structure combinatorics. *Phys. Rev. X* **7**, 041069 (2017).
60. Zhang, T. et al. Catalogue of topological electronic materials. *Nature* **566**, 475 (2019).
61. Tang, F., Po, H. C., Vishwanath, A. & Wan, X. Comprehensive search for topological materials using symmetry indicators. *Nature* **566**, 486 (2019).
62. Vergniory, M. et al. A complete catalogue of high-quality topological materials. *Nature* **566**, 480 (2019).
63. Skurativska, A., Neupert, T. & Fischer, M. H. Atomic limit and inversion-symmetry indicators for topological superconductors. *Phys. Rev. Res.* **2**, 013064 (2020).
64. Ono, S., Po, H. C. & Watanabe, H. Refined symmetry indicators for topological superconductors in all space groups. *Sci. Adv.* **6**, eaaz8367 (2020).
65. Ono, S., Po, H. C. & Shiozaki, K. $\mathbb{Z}_2$-enriched symmetry indicators for topological superconductors in the 1651 magnetic space groups. *Phys. Rev. Res.* **3**, 023086 (2021).
66. Geier, M., Brouwer, P. W. & Trifunovic, L. Symmetry-based indicators for topological Bogoliubov–de Gennes Hamiltonians. *Phys. Rev. B* **101**, 245128 (2020).
67. Tang, F., Ono, S., Wan, X. & Watanabe, H. High-throughput investigations of topological and nodal superconductors. *Phys. Rev. Lett.* **129**, 027001 (2022).
68. May, J. P. et al. *Equivariant Homotopy and Cohomology Theory: Dedicated to the Memory of Robert J. Piacenza* (American Mathematical Society, 1996).
69. Shiozaki, K. & Ono, S., Atiyah-Hirzebruch spectral sequence for topological insulators and superconductors: E2 pages for 1651 magnetic space groups. https://arxiv.org/abs/2304.01827 (2023).
70. Qi, X.-L., Hughes, T. L. & Zhang, S.-C. Topological invariants for the Fermi surface of a time-reversal-invariant superconductor. *Phys. Rev. B* **81**, 134508 (2010).
71. Fang, C., Gilbert, M. J. & Bernevig, B. A. Bulk topological invariants in noninteracting point group symmetric insulators. *Phys. Rev. B* **86**, 115112 (2012).
72. Zhang, F., Kane, C. L. & Mele, E. J. Topological mirror superconductivity. *Phys. Rev. Lett.* **111**, 056403 (2013).
73. Schnyder, A. P., Ryu, S., Furusaki, A. & Ludwig, A. W. W. Classification of topological insulators and superconductors in three spatial dimensions. *Phys. Rev. B* **78**, 195125 (2008).
74. Kitaev, A. Periodic table for topological insulators and superconductors. *AIP Conf. Proc.* **1134**, 22 (2009).
75. Ryu, S., Schnyder, A. P., Furusaki, A. & Ludwig, A. W. W. Topological insulators and superconductors: tenfold way and dimensional hierarchy. *N. J. Phys.* **12**, 065010 (2010).
76. Katayama, N. et al. Superconductivity in $Ca_{1-x}La_xFeAs_2$: A Novel 112-type iron pnictide with arsenic zigzag bonds. *J. Phys. Soc. Jpn.* **82**, 123702 (2013).
77. Sun, H. et al. Signatures of superconductivity near 80 k in a nickelate under high pressure. *Nature* **621**, 493 (2023).
78. Ko, E. K. et al. Signatures of ambient pressure superconductivity in thin film $La_3Ni_2O_7$. *Nature* **638**, 935 (2025).
79. Jiang, K., Wu, X., Hu, J. & Wang, Z. Nodeless high-T_c superconductivity in the highly overdoped CuO_2 monolayer. *Phys. Rev. Lett.* **121**, 227002 (2018).
80. Stewart, G. R. Heavy-fermion systems. *Rev. Mod. Phys.* **56**, 755 (1984).
81. Sato, M., Tanaka, Y., Yada, K. & Yokoyama, T. Topology of Andreev bound states with flat dispersion. *Phys. Rev. B* **83**, 224511 (2011).
82. Giannozzi, P. et al. Quantum espresso: a modular and open-source software project for quantum simulations of materials. *J. Phys. Condens. Matter* **21**, 395502 (19pp) (2009).
83. Giannozzi, P. et al. Advanced capabilities for materials modelling with Quantum Espresso. *J. Phys. Condens. Matter* **29**, 465901 (2017).
84. Matsugatani, A., Ono, S., Nomura, Y. & Watanabe, H. QEIRREPS: an open-source program for Quantum ESPRESSO to compute irreducible representations of Bloch wavefunctions. *Comput. Phys. Commun.* **264**, 107948 (2021).
85. Groom, C. R., Bruno, I. J., Lightfoot, M. P. & Ward, S. C. The Cambridge structural database. *Acta Crystallogr. Sect. B* **72**, 171 (2016).
86. Ahn, J. & Yang, B.-J. Unconventional Majorana fermions on the surface of topological superconductors protected by rotational symmetry. *Phys. Rev. B* **103**, 184502 (2021).
87. Kokalj, A. XCrySDen—a new program for displaying crystalline structures and electron densities. *J. Mol. Graph. Model.* **17**, 176 (1999).

Acknowledgements

Z.Z. and S.O. thank Hoi Chun Po for the support and encouragement for the project. Z.Z. thanks Shengshan Qin and Xianxin Wu, for helpful discussions. K.S. and S.O. thank Masatoshi Sato for helpful discussions. K.S., C.F., and S.O. thank the Yukawa Institute for Theoretical Physics at Kyoto University. Discussions during the YITP workshop YITP-T-24-03 on "Recent Developments and Challenges in Topological Phases" were useful to complete this work. Z.Z. was supported by the National Key R&D Program of China (Grant No. 2021YFA1401500, Hoi Chun Po). K.S. was supported by JST CREST (Grant No. JPMJCR19T2) and JSPS KAKENHI (Grant No. JP22H05118 and JP23K25794). C.F. was supported by the Chinese Academy of Sciences (Grant No. XDB33020000), National Natural Science Foundation of China (Grant No. 12325404) and the National Key R&D Program of China (Grant Nos. 2022YFA1403800 and 2023YFA1406700). S.O. was supported by the RIKEN Special Postdoctoral Researchers Program and the KAKENHI Grant No. JP23K19043 from the Japan Society for the Promotion of Science (JSPS).

Author contributions

Z.Z. and S.O. performed the theoretical and numerical calculations. K.S., C.F., and S.O. conceived the project and provided the theoretical understanding. All authors contributed to the design of the research, discussed the results, and wrote the manuscript.

Competing interests

The authors declare no competing interests.

Additional information

Supplementary information The online version contains supplementary material available at https://doi.org/10.1038/s41467-026-72811-z.

Correspondence and requests for materials should be addressed to Seishiro Ono.

Peer review information *Nature Communications* thanks Harley Scammell, and the other, anonymous, reviewer(s) for their contribution to the peer review of this work. A peer review file is available.

Reprints and permissions information is available at http://www.nature.com/reprints

Publisher's note Springer Nature remains neutral with regard to jurisdictional claims in published maps and institutional affiliations.